# Linearly polarized and time-resolved cathodoluminescence study of strain-induced laterally ordered $(InP)_2/(GaP)_2$ quantum wires

D. H. Rich,[a] Y. Tang, and H. T. Lin
*Department of Materials Science and Engineering, Photonic Materials and Devices Laboratory, University of Southern California, Los Angeles, California 90089-0241*

(Received 19 September 1996; accepted for publication 17 February 1997)

The optical properties of $(InP)_2/(GaP)_2$ bilayer superlattice (BSL) structures have been examined with linearly polarized cathodoluminescence (CL), time-resolved CL spectroscopy, and cathodoluminescence wavelength imaging. An In and Ga composition modulation of $\sim 18\%$ forms during the metalorganic chemical vapor deposition growth of short period $(InP)_2/(GaP)_2$ bilayer superlattices. Transmission electron microscopy showed a period of $\sim 800$ Å along the [110] direction, resulting in coherently strained quantum wires. A strong excitation dependence of the polarization anisotropy and energy of excitonic luminescence from the quantum wires was found. The results are consistent with a phase-space and band filling model that is based on a $\mathbf{k}\cdot\mathbf{p}$ and two dimensional quantum confinement calculation which takes the coherency strain into account. CL images reveal that defects in the BSL originate from the GaAs substrate and/or the initial stages of InGaP growth. The effects of defects on the band filling, carrier relaxation kinetics, and nonlinear optical properties were examined. © *1997 American Institute of Physics.*
[S0021-8979(97)07610-X]

## I. INTRODUCTION

The use of strained-layer epitaxy has recently shown great promise for the formation of nanostructures (quantum wires and dots). The implementation of nanostructures in lasers leads to lowered lasing threshold currents, owing to a spikelike density of states (DOS) that yields a much narrower and higher peak gain as compared to quantum well lasers.[1–7] The presence of strain in quantum heterostructures will also alter the in-plane hole masses, leading to a higher speed lasing modulation capability.[8] For quantum wires (QWRs), the momentum matrix elements depend sensitively on the electric field polarization, leading to an enhancement in the polarization dependent spontaneous emission and optical gain coefficients relative to quantum well (QW) lasers.[1,2,4] The high quality of the heterolayers and interfaces that can be achieved during a single growth step circumvents the need for post-growth etching and patterning on a nanoscale that can inevitably degrade the optical and structural quality of the nanostructure and its surrounding barriers.[6,7,9–11]

Among the *in situ* growth approaches that have yielded success in the growth of nanostructures is the growth of GaAs/AlGaAs QWs on substrates with prepatterned mesas and V grooves where the facet-dependent Al and Ga cation growth and migration rates enable lateral variations in the QW thickness and attendant confinement energies, yielding a two-dimensional (2D) or 3D confinement of carriers.[6,7,9–11] Other studies have shown that an alternating beam growth of GaAs/AlAs on misoriented substrates results in a 2D bandgap modulation via the formation of a tilted superlattice.[4,5] Recently, QWRs have been fabricated by a strain-induced lateral ordering (SILO) process which occurs spontaneously when $(GaP)_n/(InP)_n$ and $(GaAs)_n/(InAs)_n$ short-period superlattices are grown on GaAs(001) and InP(001), respectively.[12–20] The SILO approach will be the focus of this article, which follows our recent report describing the observation of nonlinear optical properties of an $(InP)_2/(GaP)_2$ bilayer superlattice (BSL) structure.[17,18] A lateral modulation of the In and Ga compositions, by as much as $\sim 30\%$, has been observed in transmission electron microscopy (TEM) and energy dispersive x-ray spectroscopy (EDS) studies.[14,16] The driving force for the long-range lateral ordering is attributed to the surface strain during the initial stages of heteroepitaxial growth and attendant spinodal decomposition during the initial stages of the BSL growth.[13,16]

Optical measurements of SILO structures using photoluminescence, electroluminescence, cathodoluminescence (CL), and photoreflectance have shown evidence supporting the existence of QWRs due to quantum confinement along both the growth direction and the composition modulation direction.[14–20] Nonlinear optical properties in such structures are expected to be enhanced due to the narrowing of the density of states (DOS) in two-dimensionally confined systems. One important nonlinear optical property is the change in the emission of light (in energy, polarization, and intensity) that results from phase-space filling of carriers.[17,18] In this study, we examine the nonlinear optical properties and carrier relaxation dynamics of $(InP)_2/(GaP)_2$ BSL samples using time-resolved CL, linearly polarized cathodoluminescence (LPCL), and cathodoluminescence wavelength imaging (CLWI) techniques. We demonstrate the existence of an excitation- and temperature-dependent polarization anisotropy in luminescence coming from the SILO quantum wires. A theoretical simulation of the band-filling, luminescence energy shifts and polarization anisotropy changes was performed for the QWRs using a $\mathbf{k}\cdot\mathbf{p}$ band-structure calculation, which takes the coherency strain and 2D quantum confinement into account. Experimental results from LPCL and

[a]Electronic mail: danrich@almaak.usc.edu



Downloaded¬27¬Feb¬2007¬to¬132.72.138.1.¬Redistribution¬subject¬to¬AIP¬license¬or¬copyright,¬see¬http://jap.aip.org/jap/copyright.jsp

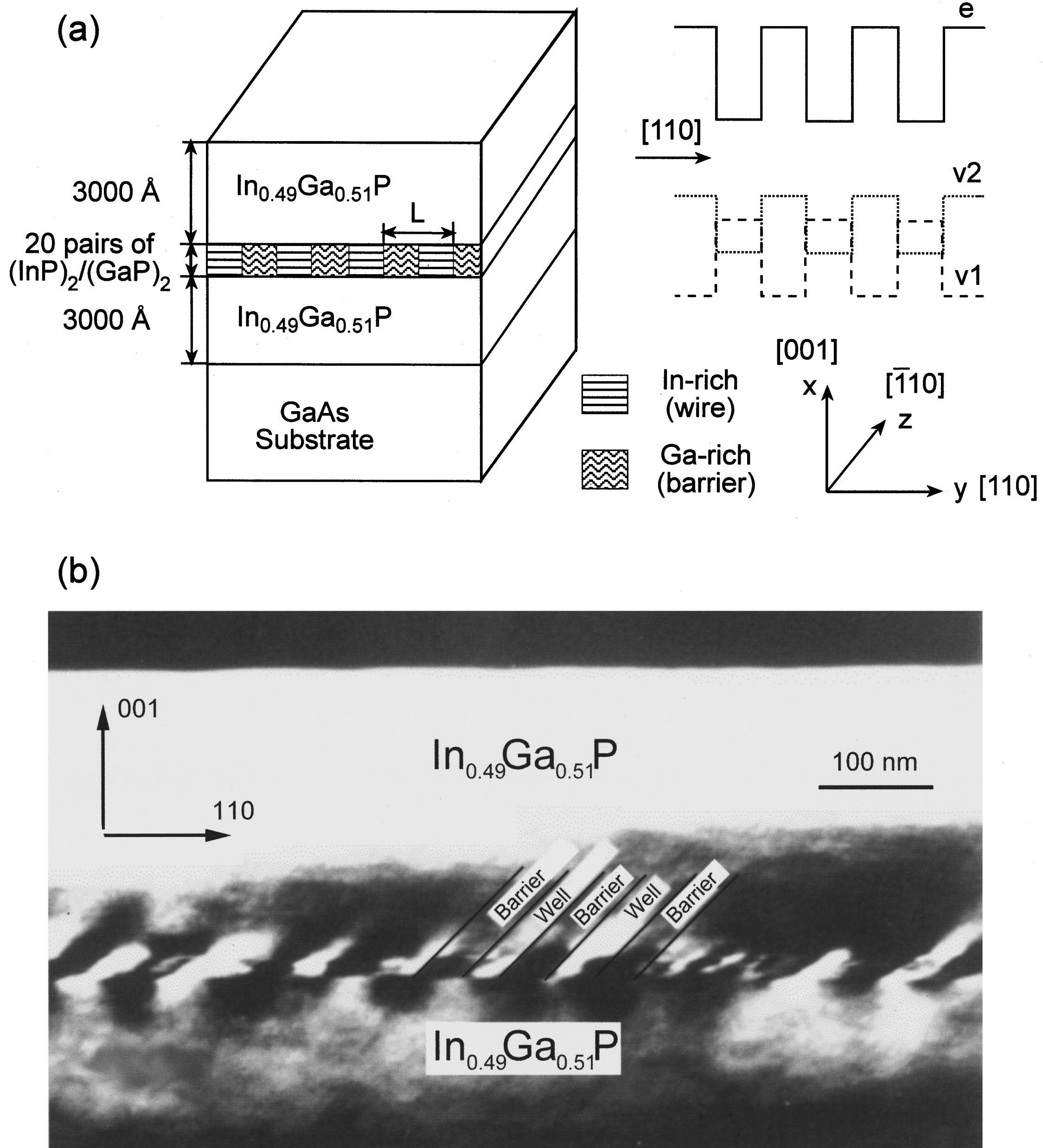


FIG. 1. (a) A schematic diagram of the $(InP)_2/(GaP)_2$ BSL and type-I to type-II superlattice modulation for $e-v1$ and $e-v2$ transitions. (b) Cross-section transmission electron micrography showing the composition modulation along the [110] direction.

excitation-dependent CL are compared with the theoretical calculations. Evidence for strong nonlinear optical effects is a cornerstone in establishing true QWR behavior and further underscores the good potential for applications in low threshold lasers and exotic light modulators.

In addition, the epitaxial growth of $In_xGa_{1-x}P$ is found to be very sensitive to the initial surface quality of the GaAs(001) substrate, its level of misorientation, the growth temperature, and growth rate.[21,22] The resulting quality and homogeneity of $(InP)_2/(GaP)_2$ QWRs are also thus expected to strongly depend on these growth conditions. We have examined the quality and reproducibility of QWRs grown on different substrates using LPCL and CLWI. The effects of defects and inhomogeneities in the BSL structure on the band filling, carrier relaxation kinetics, and nonlinear optical properties were examined.

## II. EXPERIMENT

The BSL structures in this study were grown by metal-organic chemical vapor deposition (MOCVD) at Spire Corporation. A schematic diagram of the structure is shown in Fig. 1(a). First, a 3000 Å $In_{0.49}Ga_{0.51}P$ buffer layer was grown on a GaAs(001) substrate misoriented 3° toward



Downloaded¬27¬Feb¬2007¬to¬132.72.138.1.¬Redistribution¬subject¬to¬AIP¬license¬or¬copyright,¬see¬http://jap.aip.org/jap/copyright.jsp

(111)A. The GaAs substrate was maintained at $T=650\,^{\circ}\mathrm{C}$ during growth. Each $(\mathrm{InP})_2$ and $(\mathrm{GaP})_2$ bilayer was grown in a time interval of $\sim 10$ s, after which the system was purged to prepare for the succeeding layer. A total of 20 periods of $(\mathrm{InP})_2/(\mathrm{GaP})_2$ were grown giving a thickness of $\sim 200$ Å. Finally, a 3000 Å $\mathrm{In_{0.49}Ga_{0.51}P}$ capping layer was grown. All three samples (labeled as 2979, 2980 and 2983) were grown with nominally the same growth conditions. As evidenced by the data to be presented below, slight variations in the growth condition, such as the growth rates and sample temperature, as well as the quality of the starting GaAs substrate, resulted in differences in the optical quality among the three samples. Cross-sectional TEM of sample 2979 is shown in Fig. 1(b), and reveals that the composition modulation occurred along the [110] direction with a period of $\sim 800$ Å. Previous reports on similar structures showed that the In composition varies from $\sim 0.41$ in the Ga-rich region to $\sim 0.59$ in the In-rich region.[20] Such a lateral superlattice embedded in an $\mathrm{In_{0.49}Ga_{0.51}P}$ barrier forms a multiple QWR array, as illustrated in Fig. 1(a).

The LPCL and CLWI experiments were performed with a modified JEOL-840A scanning electron microscope using a 10 keV electron beam with a probe current, $I_b$, ranging from 50 pA to 30 nA. This CL system with polarization detection capability has been previously described.[23] The sample temperature was varied between 87 and 300 K, using a liquid nitrogen cryogenic specimen stage. Light with the electric field, **E**, parallel to the [110] or $[1\bar{1}0]$ direction was detected. The luminescence signal was dispersed by a 1/4 m monochromator and detected by a cooled GaAs:Cs photo-multiplier tube (PMT) with a spectral resolution of $\sim 1$ nm. In CLWI the wavelength, $\lambda_m$, at which the intensity of luminescence is a maximum is mapped as a function of the spatial $(x,y)$ position, and a gray-scale image representing these wavelengths is generated.[24,25] A scanning area of 128 $\mu$m$\times$94 $\mu$m in this study is discretized into 640$\times$480 pixels. In order to determine $\lambda_m(x,y)$, a spectrum consisting of 45 wavelength points (obtained from 45 discrete monochromatic CL images), varying from 650 to 740 nm, was obtained at each pixel position.

Time-resolved CL experiments were performed with the method of delayed coincidence in an inverted single photon counting mode, with a time resolution of $\sim 100$ ps.[26] Electron beam pulses of 50 ns width with a 1 MHz repetition rate were used to excite the sample. The luminescence signal was dispersed by a 1/4 m monochromator and detected by a cooled GaAs:Cs PMT. Time-delayed CL spectra were acquired with a spectral resolution of $\sim 1$ nm.

## III. THEORY

In order to model nonlinear optical effects that are responsible for polarization and energy variations caused by changing the excitation conditions, the electron and hole eigenstates of the QWRs can be calculated by using a single band effective mass approximation with band parameters found using the $\mathbf{k}\cdot\mathbf{p}$ perturbation method employing a full Luttinger–Kohn (LK) and Pikus–Bir (PB) Hamiltonian, denoted as $\mathscr{H}_{\mathrm{LK}}(\mathbf{k})$ and $\mathscr{H}_{\mathrm{PB}}$, respectively.[27] The aim in this section is to describe the framework of the calculations that are used to model data showing the excitation dependence of the intensity, energy, and lineshape of polarized CL spectra which will be shown and discussed in Sec. IV. Ignoring the coupling between the conduction and valence bands, one can obtain the complete wave functions of electron and holes in a QWR whose in-plane 2D confinement of carriers is defined by $x-y$ Cartesian coordinates from the following 3D Schrödinger equation:

$$\left[\mathscr{H}_T\left(-i\frac{\partial}{\partial x},-i\frac{\partial}{\partial y},k_z\right)+V(x,y,z)\right]\psi_{e,h}(x,y,z)=E_n^{e,h}\psi_{e,h}(x,y,z), \tag{1}$$

where $\mathscr{H}_T(\mathbf{k})=\mathscr{H}_{\mathrm{LK}}(\mathbf{k})+\mathscr{H}_{\mathrm{PB}}$ is the combined Luttinger–Kohn and Pikus–Bir Hamiltonian (see Appendix) modified so as to accommodate quantum confinement along the $x$ and $y$ directions; $\psi_{e,h}(x,y,z)$ is the electron or hole wave function; $E_n^{e,h}$ is the eigen-state energy. The modification of $\mathscr{H}_T$, in the effective mass approximation (EMA), simply entails replacing $k_x$ and $k_y$ with $-i\partial/\partial x$ and $-i\partial/\partial y$, respectively, resulting in a set of six coupled second-order linear partial differential equations. Owing to the computational complexity of getting exact solutions of Eq. (1) for an arbitrary strain tensor and boundary conditions for the potential and wave functions, it is desirable to simplify the treatment. Since the strain profile in QWR structures is complicated and many uncertainties in the nanometer-scale structure remains, a simplified, single-band EMA treatment is desirable here. Therefore, we make the following assumptions:

- (i) free-electron-like and free-hole-like solutions are assumed for motion along the QWR direction [i.e., $\psi_{e,h}(z)=\exp(ik_z z)$ and $E_z^{e,h}=\hbar^2k_z^2/2m_z^{e,h}$],
- (ii) the coupling between orthogonal eigenstates is ignored, i.e., $\psi_{e,h}(x,y)\approx\psi_{e,h}(x)\psi_{e,h}(y)$, as can be verified for a relatively large dimension quantum wire greater than $\sim 100$ Å$\times$100 Å,[28] and
- (iii) a rectangular approximation is used for the $x-y$ potential profile $V_{c,v}(x,y)$ and effective mass, which can be determined by the $\mathbf{k}\cdot\mathbf{p}$ calculation discussion above.

Equation (1) can then be separated into two ordinary differential equations for $x$ and $y$, and the quantized energy levels, $E_n^{e,h}$, can be solved separately for the two confinement directions as $E_n^{e,h}=E_{x,i}^{e,h}+E_{y,j}^{e,h}$, using a transfer matrix method (TMM). The TMM was demonstrated to be very efficient in solving the Schrödinger equation with an arbitrary one-dimensional potential.[29,30]

Using these eigenstates, quasi-Fermi energies for electrons and holes can be determined for a given excess carrier concentration, $n_q$, to simulate the effects of band filling. The electron and hole carrier densities, $n_i^{e,h}$, in these quantized states can be determined by integrating the product of the 1D density of states and the Fermi–Dirac function, $f(E-\phi_{e,h})$, for electrons and holes. The quasi-Fermi levels, $\phi_{e,h}$, are determined by solutions of the following equations:



Downloaded¬27¬Feb¬2007¬to¬132.72.138.1.¬Redistribution¬subject¬to¬AIP¬license¬or¬copyright,¬see¬http://jap.aip.org/jap/copyright.jsp

$$n_i^{e,h} = \int_{E_i}^{\infty} \frac{dE}{\pi L_x L_y} \left( \frac{2m_z^{e,h}}{\hbar^2} \right)^{1/2} \frac{f(E-\phi_{e,h})}{\sqrt{E-E_i^{e,h}}};$$

$$n_q = \sum_i n_i^e = \sum_i n_i^h, \tag{2}$$

where $L_x$ and $L_y$ are the dimensions of the quantum wire, and $m_z^{e,h}$ is the effective mass along $[1\bar{1}0]$ ($z$ direction). The luminescence lineshape, $I(\hbar\omega)$, can further be calculated from

$$I(\hbar\omega) = \sum_{i,j} I_{ij}^2 \int_{E_i^e}^{\hbar\omega - E_g - E_j^h} dE\ H(\hbar\omega - E_g - E_i^e - E_j^h) g_J(\hbar\omega) f(E-\phi_e) f(\hbar\omega - E_g - E - \phi_h),$$

$$g_J(\hbar\omega) = \frac{1}{\pi\sqrt{2}\hbar} \frac{\sqrt{m_r}}{\sqrt{\hbar\omega - E_g - E_i^e - E_j^h}}, \tag{3}$$

where $H(E)$, the Heaviside function, is 0 for $E<0$ and is 1 for $E \geqslant 0$, $I_{ij}$ is the overlap integral for electron and hole envelope wave functions, i.e., $I_{ij} = \int d^2\mathbf{r} \psi_{i,e}(x,y) \psi_{j,h}(x,y)$, and $g_J(\hbar\omega)$ is the joint density of states for $k_z$-conserving interband transitions in quantum wires, which contains the reduced mass term $m_r$, where $1/m_r = 1/m_z^e + 1/m_z^h$. Using the calculated values for the quasi-Fermi levels, we have calculated $I(\hbar\omega)$ as a function of carrier density. In addition, to include the effects of instrumental and inhomogeneous broadening, we have convolved $I(\hbar\omega)$ with a Gaussian of width equal to the width of the narrowest optical transition, which was measured for the lowest probe current, i.e.,

$$L(\hbar\omega) = \int_0^{\infty} d(\hbar\omega') I(\hbar\omega') \exp\left( -\frac{(\hbar\omega - \hbar\omega')^2}{\beta^2} \right). \tag{4}$$

Furthermore, the polarization dependence of the luminescence from the QWRs can be calculated as a function of excitation density and temperature. Since $g_J(\hbar\omega)$ is singular for the lowest energy optical transitions, the largest polarization anisotropy is dominated by states with $k_z=0$, which occur for the lowest excitation conditions. From the overlap integrals, $I_{ij}$, and the calculated conduction and valence Bloch functions, we can calculate the polarization dependent transition matrix elements. The integrated intensity of polarized luminescence is determined by the carrier occupation densities and the electron-hole wavefunction overlap according to

$$I_{\perp,\parallel} = \sum_{i,j} n_i^e n_j^h |I_{ij} \langle u_{i,c} | \mathbf{E}_{\perp,\parallel} \cdot \mathbf{p} | u_{j,v} \rangle|^2, \tag{5}$$

where $\mathbf{E}_{\perp,\parallel}$ is the electric field of emitted light which is detected either along the $[110]$ ($\perp$) or $[1\bar{1}0]$ ($\parallel$) direction, $\mathbf{p}$ is the linear momentum operator, and $u_{i,c}$ and $u_{j,v}$ are the set of band-edge conduction and valence band Bloch functions, the latter of which is a linear combination of the six $|J,m_j\rangle$ states in the $\langle 110 \rangle$ representation as determined from the Luttinger–Kohn and Pikus–Bir Hamiltonian (see Appendix).

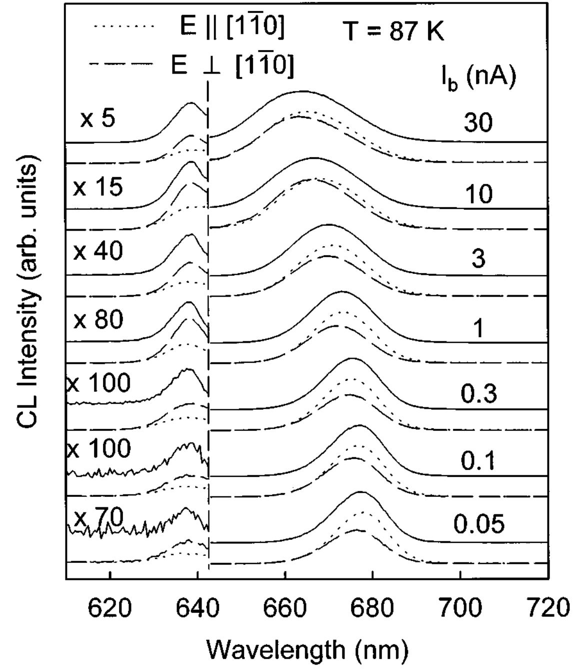


FIG. 2. Stack plots of normalized spatially-integrated non-polarized (solid line) and polarized (dashed lines) CL spectra taken for different probe currents at $T=87$ K.

## IV. RESULTS AND DISCUSSION OF AN OPTICALLY HOMOGENOUS QWR SAMPLE

### A. Linearly polarized CL spectroscopy

Polarized and nonpolarized CL spectra were taken as a function of probe current in sample 2979, as shown in Fig. 2 for a temperature of 87 K. In the wavelength range between 620 and 720 nm, two peaks, respectively, originating from the QWR and $In_{0.49}Ga_{0.51}P$ bulk (i.e., the buffer and capping layers) are observed. CL imaging of this sample in Fig. 3, with wavelengths corresponding to emissions from (a) the QWR and (b) $In_{0.49}Ga_{0.51}P$ barriers, shows a high degree of homogeneity. The peak energy of the $In_{0.49}Ga_{0.51}P$ bulk emission remains almost constant ($\sim$1.950 eV) for the different probe currents in Fig. 2. Emission from the QWR has a lower energy compared to that from the $In_{0.49}Ga_{0.51}P$ layers, as the lateral composition modulation along $[110]$ results in $\sim$400 Å×200 Å quantum wires composed of an In-rich $(GaP)_2/(InP)_2$ BSL region. The QWR peak energy shifts from 1.834 to 1.869 eV as $I_b$ increases from 50 pA to 30 nA, as observed in Fig. 2 and plotted (with dots) vs $I_b$ in Fig. 4. This nonlinear optical behavior shows that the confined states in the QWR can be filled by a fairly low electron beam excitation. A narrower density of states is expected as the dimensionality of the quantum confinement increases from 1D to 2D. We hypothesize that the SILO formation of quantum wires in the BSL leads to the enhanced phase-space filling and nonlinear optical effects.

To further test this hypothesis, we have examined the polarization dependence of the luminescence in detail. The luminescence from $In_{0.49}Ga_{0.51}P$ bulk is polarized along the $[110]$ direction and the magnitude of such polarization does not change for different probe currents and temperatures.



Downloaded¬27¬Feb¬2007¬to¬132.72.138.1.¬Redistribution¬subject¬to¬AIP¬license¬or¬copyright,¬see¬http://jap.aip.org/jap/copyright.jsp

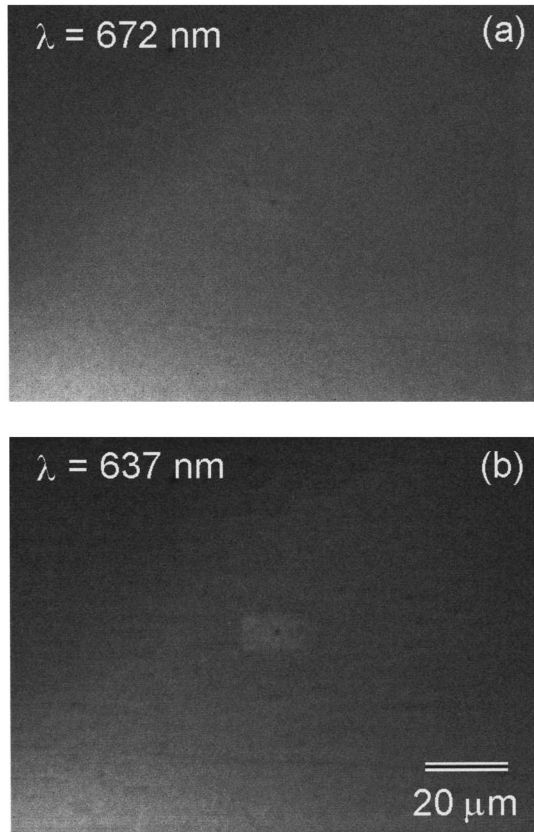


FIG. 3. Monochromatic CL images of (a) the QWR and (b) $In_{0.49}Ga_{0.51}P$ barrier luminescence of sample 2979, showing uniformity in its optical properties.

This is consistent with a CuPt-like ordering which is found to occur along the $[\bar{1}11]$ or $[1\bar{1}1]$ direction of an epitaxially grown $In_{0.49}Ga_{0.51}P$ layer.[21,22,31–33] On the other hand, the polarization of emission from the QWRs has an orthogonal orientation and greatly depends on the probe current and temperature, as shown in Figs. 2 and 5. With an increase in probe current from 50 pA to 30 nA, the polarization ratio (or

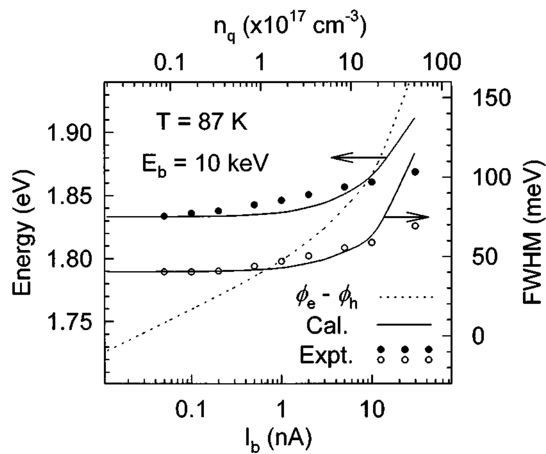


FIG. 4. Experimental and calculated energies of the peak CL intensity position, $E_P$ (closed circle), full width at half maximum (FWHM) of luminescence lineshape (open circle), and calculated quasi-Fermi level difference (dash lines) vs the excitation density ($n_q$) and probe current ($I_b$).

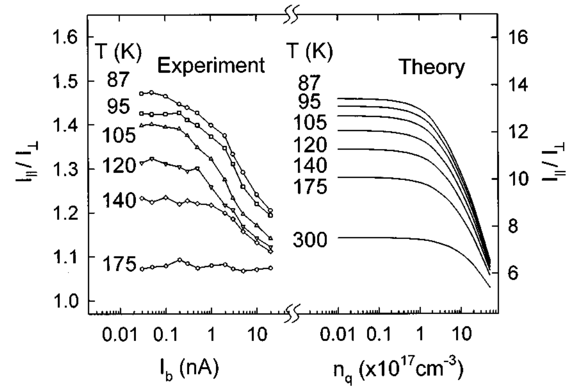


FIG. 5. Experimental and theoretical polarization ratios, $I_\parallel/I_\perp$, as a function of the excitation density for sample 2979. Parallel and perpendicular subscripts are defined with respect to the $[1\bar{1}0]$ quantum wire direction.

optical anisotropy) $I_\parallel/I_\perp$, which is defined as the ratio of integrated CL intensities with electric field **E** parallel and perpendicular to the $[1\bar{1}0]$ quantum wire directions, reduces from $\sim 1.5$ to 1.1 at a temperature of 87 K. Under a fixed $I_b$, the polarization ratio decreases as the temperature increases, as shown in Fig. 5. These changes of polarization with probe current and temperature are consistent with the band-filling model.

## B. Application of theory to experimental results

The QWRs are assumed to be coherently strained so that their in-plane lattice constant, $a_\parallel$, is equal to that of GaAs. Assuming a biaxial strain on the (110) interfacial plane between In-rich and Ga-rich regions, we obtain the strain tensor in the $\langle 100 \rangle$ representation for each $In_{0.49}Ga_{0.51}P$ ($x=0.41$ or 0.59) region of the BSL as follows:

$$\epsilon_{11}=\epsilon_{22}=\frac{2C_{44}-C_{12}}{C_{11}+C_{12}+2C_{44}}\,\epsilon_\parallel,$$

$$\epsilon_{12}=-\frac{C_{11}+2C_{12}}{C_{11}+C_{12}+2C_{44}}\,\epsilon_\parallel,\quad \epsilon_{23}=\epsilon_{31}=0,\quad \epsilon_{33}=\epsilon_\parallel, \tag{6}$$

where $C_{11}$, and $C_{12}$ and $C_{44}$ are elastic stiffness constants of $In_{0.49}Ga_{0.51}P$, $\epsilon_\parallel=(a_\parallel-a_i)/a_i$ is the (001) in-plane strain, and $a_i$ is the unstrained lattice constant for either the In- or Ga-rich regions of the BSL, using a pseudo-alloy approximation. The Luttinger parameters, deformation potentials, elastic constants, and spin-orbit splitting were approximated using a linear interpolation between values which are known for GaP and InP.[20] The diagonalization of the Hamiltonian $\mathscr{H}_T(k_x,k_y,k_z)$ results in the $E$ vs **k** bulk-band dispersion for electrons and holes and enables a determination of the set of strain-split valence band Bloch functions, which contain admixtures of the $|3/2,\pm 3/2\rangle$, $|3/2,\pm 1/2\rangle$, and $|1/2,\pm 1/2\rangle$ states, owing to the magnitude and low symmetry of the strain. The conduction to valence band offset ratio $(\Delta E_c/\Delta E_v)$ is taken as 75/25, and is assumed independent of the alloy composition.[34] This results in type-I and type-II superlattices for the two uppermost valence bands, $v1$ and $v2$, as shown in Fig. 1(a), in the In- and Ga-rich regions,



Downloaded¬27¬Feb¬2007¬to¬132.72.138.1.¬Redistribution¬subject¬to¬AIP¬license¬or¬copyright,¬see¬http://jap.aip.org/jap/copyright.jsp

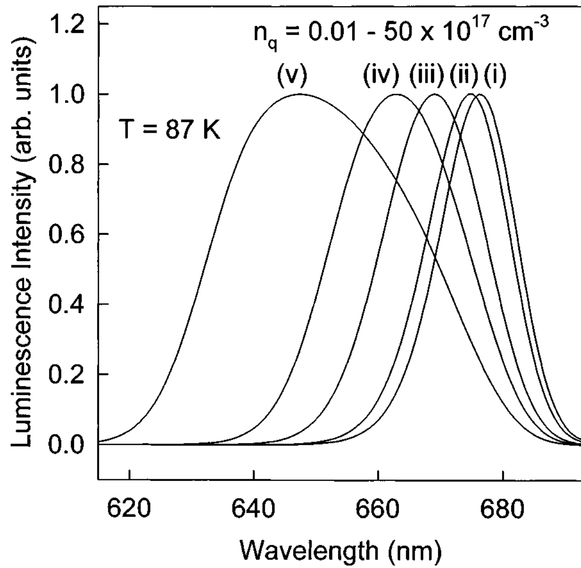


FIG. 6. Calculated luminescence lineshapes for (i) 0.01, (ii) 2, (iii) 10, (iv) 20, and (v) $50\times10^{17}$ cm$^{-3}$ showing blue shift and broadening of the FWHM peak with increasing excess carrier concentration.

respectively, which have characters that are 96% heavy-hole (hh; $m_j=\pm3/2$) and 94% light-hole (lh; $m_j=\pm1/2$) in the $\langle110\rangle$ representation. Other salient features of the calculation are that $\Delta E_c=120$ meV, $\Delta E_v=40$ meV for the $v1$ bands, and $v1$ and $v2$ are split by 42 and 48 meV in the In- and Ga-rich regions, respectively. Since $e-v1$ and $e-v2$ transitions are spatially direct and indirect transitions, respectively, the relative contribution of $e-v1$ and $e-v2$ optical transitions should involve an interplay between the electron-hole wave function overlap and carrier occupation density. The $e-$hh and $e-$lh transitions, in strained and quantum confined systems, will generally exhibit an orthogonal polarization dependence. By altering the relative contributions of the $e-v1$ and $e-v2$ transitions in the luminescence, which can be accomplished by changing the excitation density (i.e., probe current here), a variation in the polarization ratio is thus expected.

A quantitative analysis was performed as discussed in Sec. III under the coherency strain condition. In this calculation all bound states were included and resulted in 21 electron, 45 $v1$ and 20 $v2$ states. The luminescence lineshapes were calculated from Eqs. (3) and (4) found to be a function of carrier concentrations, as shown in Fig. 6. The position of maximum peak intensity of $I(\hbar\omega)$, $E_p$, and the difference between the quasi-Fermi energies of electrons and holes, $\phi_e-\phi_h$, are plotted versus $n_q$ in Fig. 4, and show a reasonable agreement with the experimental QWR peak position and width. As the quasi-Fermi level difference increases with increasing probe current, optical transitions with higher energies contribute to the luminescence spectrum, resulting in the observed blue-shift in the QWR peak. In addition, more higher energy states are involved in the luminescence causing the broadening with increasing excitation density. The full width at half maximum (FWHM) of luminescence lineshape is plotted in Fig. 4 in comparison with the experimental results. The relationship between carrier concentration $n_q$ and probe current $I_b$ is given by

$$n_q\approx\frac{I_bE_b\tau_{\mathrm{QWR}}}{3eE_g\pi r_e^2T_{\mathrm{BSL}}}, \tag{7}$$

where $E_b$ is the $e$-beam energy, $E_g$ is the $In_{0.49}Ga_{0.51}P$ band gap, $r_e$ is the effective lateral radius of the electron-hole plasma generated by the $e$-beam, $\tau_{\mathrm{QWR}}$ is the electron-hole radiative recombination lifetime in the QWR, and $T_{\mathrm{BSL}}$ ($\approx200$ Å) is the BSL thickness. Using $E_g\approx1.950$ eV, $r_e\approx1$ $\mu$m, and $\tau_{\mathrm{QWR}}\approx1$ ns (see Sec. IV C),[35] we get $n_q(\mathrm{cm}^{-3})=1.7\times10^{17}I_b(\mathrm{nA})$. In Eq. (7), we assume that all the generated excess carriers are collected into the BSL layer. The value of $\tau_{\mathrm{QWR}}$ used is only approximate; this lifetime is expected to depend on the $e-h$ excitation density as the occupation of higher energy electron and hole states will affect the number of interband matrix elements used in a lifetime calculation.[30] Further, thermal re-emission of carriers should increase under increased excitation and, particularly, at higher temperatures, since the effective barrier (difference between the quasi-Fermi and unbound continuum levels) decreases with increasing excitation.

A calculated polarization ratio $I_\parallel/I_\perp$ as a function of probe current and temperature, based on the diagonalization of $\mathscr{H}_T(\mathbf{k})$ and the phase-space filling effects discussed in Sec. III, is shown in Fig. 5, and is compared with the experimental results. For our strained QWRs, the diagonalization of $\mathscr{H}_T(\mathbf{k})=\mathscr{H}_{\mathrm{LK}}(\mathbf{k})+\mathscr{H}_{\mathrm{PB}}$ at $k_z=0$ will yield a ground-state $e1-v1$ transition whose final hole states are of mixed hh and lh characters (as discussed above) and a polarization ratio $I_\parallel/I_\perp$ which is either greater than or less than unity as determined by the interplay of quantum confinement and strain in $\mathscr{H}_{\mathrm{LK}}(\mathbf{k})$ and $\mathscr{H}_{\mathrm{PB}}$, respectively. The general features of the experiment and theory in Fig. 5 are quite consistent, regarding the excitation-induced reduction in polarization anisotropy, and thus confirm that our phase-space filling and SILO quantum wire model reasonably explains the nonlinear optical behavior observed in the LPCL data. Deviations between experiment and theory can largely be traced to the optical collection system used in the experiment, as the ellipsoidal mirrors, which collects off-normal emission, causes a polarization mixing that results in a maximum $I_\parallel/I_\perp$ of $\sim4$.[23]

### C. Time-resolved CL, carrier thermalization in the QWRs, and excitation-dependent changes in the QWR luminescence

In order to examine the relaxation and collection of carriers into the QWRs, we have measured time-delayed CL spectra at $T=87$ K for the various time-windows indicated in Fig. 7. The time windows O1–O6 and D1–D7 denote time windows relative to the beginning of *onset* and *decay*, respectively, of the luminescence, as referred to the beginning and end of the electron beam pulses. The ratio of the integrated CL intensities of the QWR ($650\leq\lambda\leq690$ nm) and $In_{0.49}Ga_{0.51}P$ ($625\leq\lambda\leq645$ nm) emissions, $I_{\mathrm{QWR}}/I_{\mathrm{InGaP}}$, increases from $\sim26$ to $\sim47$ during the onset of luminescence in the O1–O6 time windows. The rapid rise of the QWR



Downloaded¬27¬Feb¬2007¬to¬132.72.138.1.¬Redistribution¬subject¬to¬AIP¬license¬or¬copyright,¬see¬http://jap.aip.org/jap/copyright.jsp

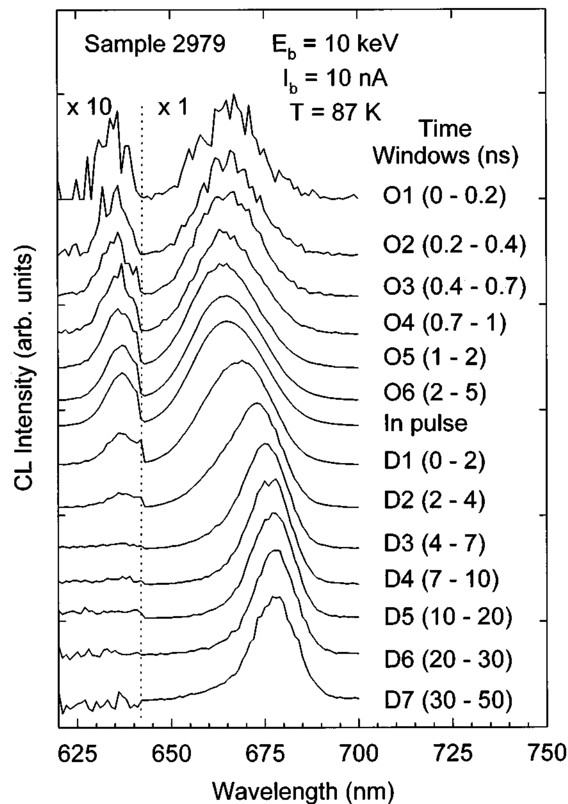


FIG. 7. Time-delayed CL spectra (sample 2979) shown with various onset (O*i*) and decay (D*i*) time windows. All spectra are renormalized to have about the same maximum peak height. The spectrum labeled *in pulse* was acquired in the center of the 50 ns *e*-beam pulse, after the system has nearly reached steady-state conditions.

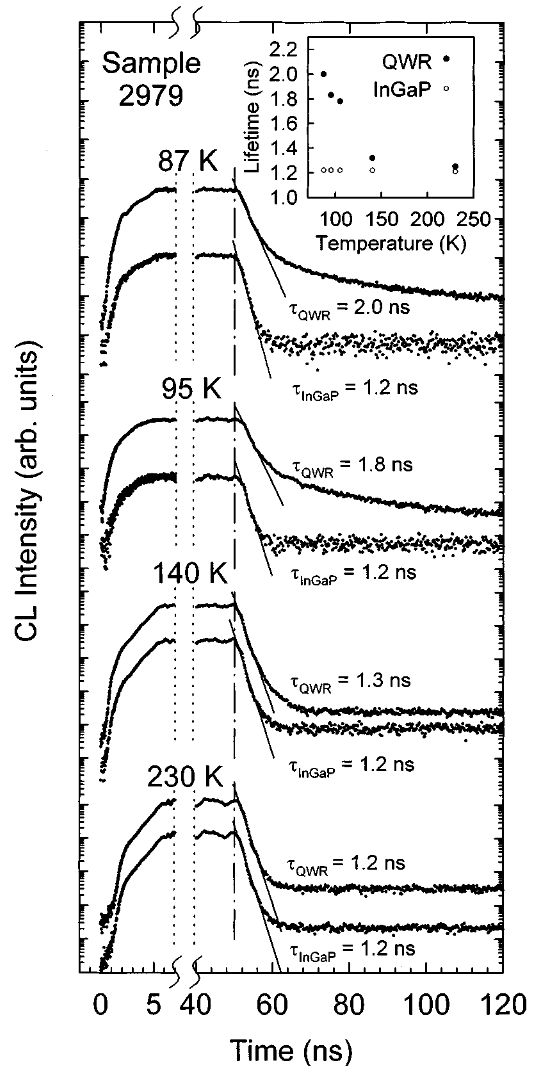


FIG. 8. CL transients of the QWR and $In_{0.49}Ga_{0.51}P$ barrier luminescence for various temperatures from 87 to 230 K. The resulting initial decay times, $\tau$QWR and $\tau_{InGaP}$, are shown vs temperature in the inset.

peak at the shortest window O1 (centered at 100 ps) reflects the rapid transfer of the carriers into the QWRs, which occupy only $\sim 2\%$ of the material within the *e*-beam excitation volume. As the time window moves from O1 to O6, the QWR peak becomes blue-shifted by $\sim 3$ nm, indicating that carrier filling of the QWR bands and splitting of the quasi-Fermi levels occurs during carrier capture into the QWR. On the other hand, the $In_{0.49}Ga_{0.51}P$ emission shifts to the red by $\sim 5$ nm in the O1–O6 time windows, reflecting the thermalization and carrier diffusion into lower-energy states of the $In_{0.49}Ga_{0.51}P$ barriers. The spectrum labeled *in pulse*, was taken in the center of the 50-ns-wide *e*-beam pulse, and represents the CL spectrum after carrier generation and recombination has reached steady-state, as in the constant-excitation CL spectra of Fig. 2.

During the decay stage of the luminescence, a narrowing and red-shifting of both the QWR and $In_{0.49}Ga_{0.51}P$ barrier emissions are observed in the D1–D3 time windows in Fig. 7 As expected, the $e-h$ plasma continuously feeds the lower energy states in both the QWR and barriers as systems proceeds towards equilibrium. The barrier emission decays more rapidly in windows D1–D4, owing to the high quantum capture rate into the QWR, as also observed in the onset windows. The CL intensity versus time transients are shown in Fig. 8 for various different sample temperatures. An initial luminescence decay time $\tau$ is measured from the slopes of the semi-logarithmic plots for both the QWR and InGaP barrier luminescence and labeled $\tau_{QWR}$ and $\tau_{InGaP}$, respectively. From the inset of Fig. 8, $\tau_{QWR}$ decreases from 2.0 to 1.2 ns, as the temperature increases from 87 to 230 K. The barrier luminescence, on the other hand, has a relatively constant lifetime of $\tau_{InGaP}=1.2$ ns over this temperature range. This lifetime behavior reveals salient aspects of the thermalization of carriers in the QWR and barriers before recombination. At high temperatures, as in MQW systems,[36,37] carriers can be thermally re-emitted from the QWR prior to their recombination. The rate of thermal re-emission of electrons and holes depends on the quasi-Fermi levels and band-offsets, which together yield the effective barrier heights. At lower temperatures, fewer carriers are thermally re-emitted, and carriers collected from the barrier recombine mainly in the QWR through radiative recombination. At higher temperatures, additional channels exist for recombination via thermal re-emission from the QWR into the barriers, thereby reducing the measured decay time.

We also measured the ratio of CL intensity emitted from different layers as a function of probe current. The ratios



Downloaded¬27¬Feb¬2007¬to¬132.72.138.1.¬Redistribution¬subject¬to¬AIP¬license¬or¬copyright,¬see¬http://jap.aip.org/jap/copyright.jsp

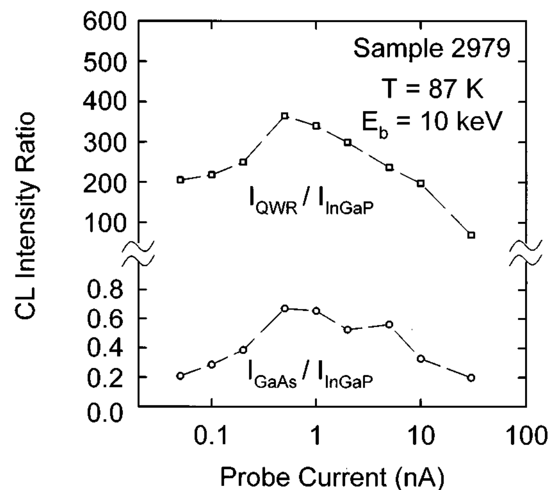


FIG. 9. CL intensity ratios, $I_{QWR}/I_{InGaP}$ and $I_{GaAs}/I_{InGaP}$, vs $e$-beam current for sample 2979.

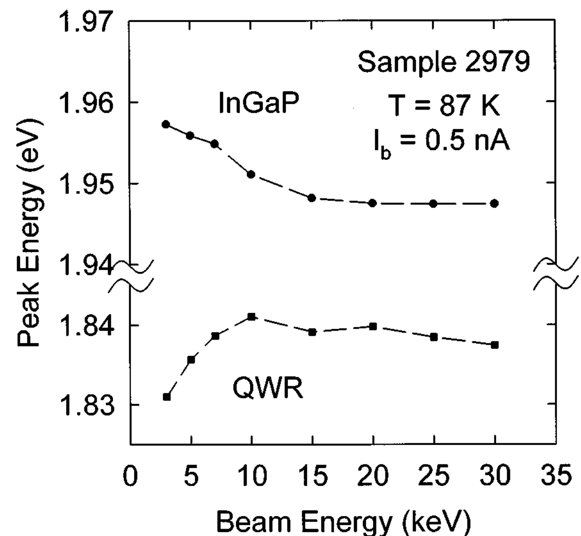


FIG. 10. Peak energies of CL emission intensity, $E_P$, from the $In_{0.49}Ga_{0.51}P$ barriers and QWR luminescence in sample 2979 as a function of $e$-beam energy.

$I_{QWR}/I_{InGaP}$ and $I_{GaAs}/I_{InGaP}$, as shown in Fig. 9, have a maximum at the intermediate probe current of $\sim$1 nA. At low excitation, most of the excess carriers diffuse into the QWR from the InGaP barriers before they recombine as is evident from the large ratios in Fig. 9. As the probe current increases from 50 pA to $\sim$1 nA, an increased fraction of carriers diffuse into the QWR and GaAs substrate, causing an increase in the intensity ratios. It is plausible that the initial rise in the $I_{QWR}/I_{InGaP}$ and $I_{GaAs}/I_{InGaP}$ ratios is due to an enhanced mobility of carriers that arises from an excitation-induced screening of local depletion regions associated with impurities and point defects in the $In_{0.49}Ga_{0.51}P$ barriers,[38] thereby giving rise to a concomitant increase in carrier collection efficiency in the QWR and carrier transfer to the GaAs substrate. An enhanced diffusivity of excess carriers as the excitation density is increased as has previously been observed in $In_xGa_{1-x}As$/GaAs MQWs.[30] However, beyond a certain excitation density, the ratios reduce as phase-space filling of the QWR states inhibits carrier capture into the QWR. Likewise, captured carriers may also be thermally re-emitted from the QWR into the $In_{0.49}Ga_{0.51}P$ barriers at higher excitation densities given that the effective barrier height for thermal re-emission is reduced due to the splitting of the electron and hole quasi-Fermi levels, as discussed above. The rates of electron and hole capture into the QWR should vary with the quasi-Fermi level positions as resonances for quantum capture depend on the availability of unoccupied final states in the QWR.[39] The $I_{GaAs}/I_{InGaP}$ ratio roughly follows the $I_{QWR}/I_{InGaP}$ behavior, indicating that carrier transfer into the GaAs substrate may be inhibited by excitation-induced changes in band-bending near the $In_{0.49}Ga_{0.51}P$/GaAs interface for higher probe currents.

As previously indicated, the CL image of Fig. 3 shows a homogeneous luminescence distribution in the sample surface plane. In order to probe the homogeneity along the growth direction, the $e$-beam energy was varied to give a depth profile of the QWR and $In_{0.49}Ga_{0.51}P$ luminescence. The data reveal a slight difference between $In_{0.49}Ga_{0.51}P$ luminescence in the capping and buffer layers. As shown in Fig. 10, the peak energy of $In_{0.49}Ga_{0.51}P$ luminescence decreases from 1.957 to 1.948 eV when $E_b$ is increased from 3 to 15 keV. The lower and higher beam energies give rise to luminescence weighted largely from the capping and buffer layers, respectively. The $In_{0.49}Ga_{0.51}P$ buffer layer was grown on a high-quality GaAs(001) surface while the capping layer was grown on the BSL layers, exhibiting the $\sim$800 Å periodic QWR ordering. Thus, the starting surface morphology for the $In_{0.49}Ga_{0.51}P$ capping and buffer layers are different and should give rise to significant differences in the degree of CuPt-like ordering. Previous studies have shown that substrate surface misorientation and homogeneity can markedly affect the CuPt-like ordering and resulting band gap.[21,22,31–33] The ordering reduces the band gap by as much as $\sim$100 meV,[21] possibly as a result of an $L$-point folding that repels the band edge at the $\Gamma$-point.[33] The 9 meV increase in the $In_{0.49}Ga_{0.51}P$ luminescence energy as the beam energy is reduced from 15 to 3 keV therefore suggests that there is a reduced ordering in the $In_{0.49}Ga_{0.51}P$ capping layer relative to the $In_{0.49}Ga_{0.51}P$ buffer layer, consistent with an expected rougher surface morphology for $In_{0.49}Ga_{0.51}P$ growth on the QWRs. The increase in the QWR peak energy as $E_b$ increases from 3 to 10 keV is a band filling effect that results from moving the center of the $e-h$ excitation volume towards the BSL layer and increasing the $e-h$ density as $E_b$ increases.

## V. RESULTS AND DISCUSSION FOR QWR SAMPLES EXHIBITING DISORDER

### A. Linearly polarized CL imaging and spectroscopy

Linearly polarized CL spectra were acquired for all three samples (2979, 2980 and 2983), as shown in Fig. 11. The difference in $In_{0.49}Ga_{0.51}P$ peak emission energies among the three samples indicates that there may be slight differences in $In_{0.49}Ga_{0.51}P$ composition, growth temperature, growth rate, or substrate surface conditions prior to and during the



Downloaded¬27¬Feb¬2007¬to¬132.72.138.1.¬Redistribution¬subject¬to¬AIP¬license¬or¬copyright,¬see¬http://jap.aip.org/jap/copyright.jsp

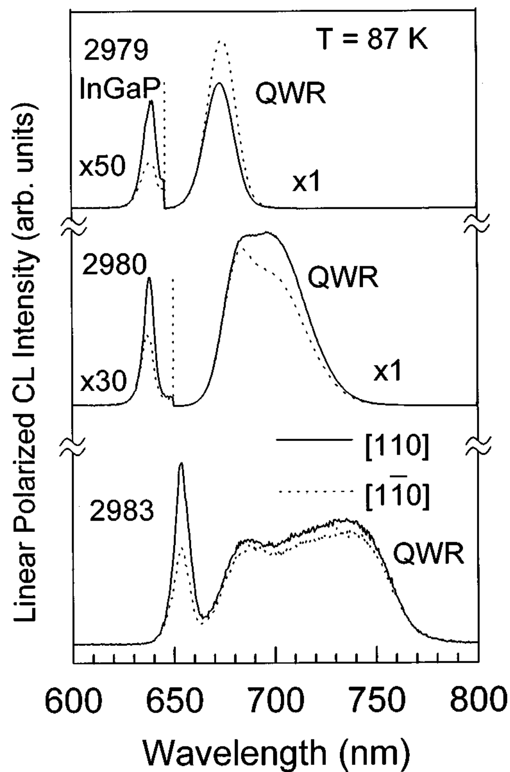


FIG. 11. Polarized CL spectra from all three QWR samples: 2979, 2980, and 2983 at $T = 87$ K.

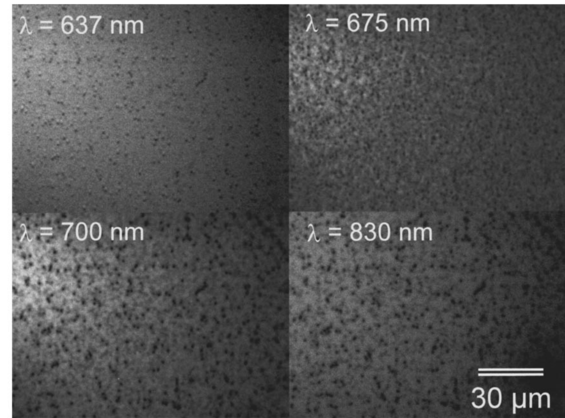


FIG. 12. Monochromatic CL images of sample 2980 with wavelengths of 637 nm ($In_{0.49}Ga_{0.51}P$ barriers), 675 and 700 nm (QWR emission), and 830 nm (GaAs substrate), respectively.

initial phases of growth. As mentioned earlier, there are two types of submicron-sized domains in the $In_xGa_{1-x}P$ grown epitaxially on GaAs substrate, with CuPt-like ordering directions along $[\bar{1}11]$ and $[1\bar{1}1]$.[21,22,31–33] The density and/or size of these domains determines the luminescence peak position while the degree of ordering affects the rate of $In_xGa_{1-x}P$ peak shift with increasing excitation density.[21] Thus, slight difference in growth conditions could result in variations in ordering and, concomitantly, in the effective band gaps. Besides the variation of peak energies, the surface morphology is found to vary among the samples. Scanning electron microscopy revealed a rough surface on sample 2983, indicating a high density of domains, consistent with the lowest $In_xGa_{1-x}P$ emission energy among the three samples.[21,22] Monochromatic CL images of sample 2980 in Fig. 12 show a spotty disorder pattern and exhibit a high-defect/spot density of $\sim 10^8$ cm$^{-2}$. The samples exhibiting disorder in the CL imaging (2980 and 2983) also show broad multicomponent peaks in the spectral range corresponding to the QWR emission ($655 \leqslant \lambda \leqslant 780$ nm) in Fig. 11. These features are evidently related to the disorder observed in the CL images. Monochromatic CL images were taken over the same 128 $\mu$m$\times$94 $\mu$m region in sample 2980 with emission wavelengths corresponding to the GaAs substrate (830 nm), QWRs (675 and 700 nm), and $In_{0.49}Ga_{0.51}P$ barrier layers (637 nm), as shown in Fig. 12. Again, a high defect density of $10^7 - 10^8$ cm$^{-2}$ is observed. A spatial correlation of defects among these images indicates that they arise probably from defects formed during the initial stages of growth on the GaAs substrate. Hageman *et al.*,[21] using microprobe analysis, have found evidence that defects in the $In_xGa_{1-x}P$/GaAs(001) growth are caused by an initial adsorption and agglomeration of In on the GaAs substrate. These defects appear to affect locally the QWR formation in the BSL, as the spots in each CL image are spatially correlated. The presence of dark spots in the CL imaging is consistent with the nonradiative recombination that may occur at the boundaries of the CuPt-like ordered domains, as the interfaces between domains could give rise to a high nonradiative recombination rate.[40] Anti-phase boundaries, which involve neighboring In and Ga planes in the $In_xGa_{1-x}P$ growth,[21,41] could also give rise to regions exhibiting high nonradiative rates. The wavelength of the $In_{0.49}Ga_{0.51}P$ barrier emission, however, was not found to vary between bright (B) and dark (D) regions as shown in Fig. 13 for two typical local spectra. These defects appear to primarily introduce recombination centers without significantly affecting the

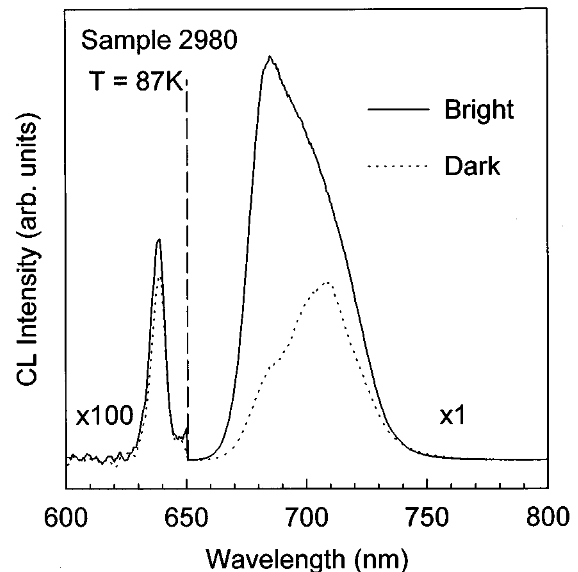


FIG. 13. Local CL spectra taken from the bright (B) and dark (D) regions in sample 2980.



Downloaded¬27¬Feb¬2007¬to¬132.72.138.1.¬Redistribution¬subject¬to¬AIP¬license¬or¬copyright,¬see¬http://jap.aip.org/jap/copyright.jsp

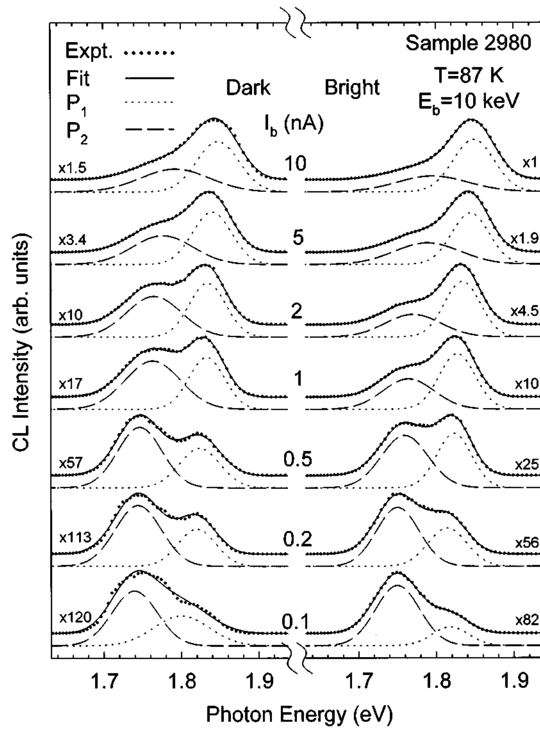


FIG. 14. Constant excitation CL spectra from localized dark and bright regions in sample 2980 for various $e$-beam currents. The results of the decomposition of the data into two components ($P_1$ and $P_2$), using fits to Eq. (8), is shown.

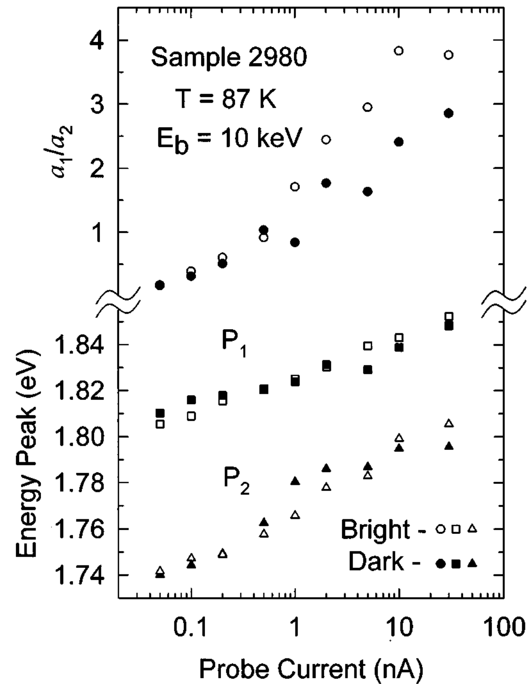


FIG. 15. Plots of the fitting parameters of Eq. (8), $a_1/a_2$, $E_1$ and $E_2$ vs $e$-beam current in both bright (open symbols) and dark (closed symbols) regions.

CuPt-like ordering, as significant changes in the ordering are expected to cause variations in the $In_{0.49}Ga_{0.51}P$ band gap.[21,22,31–33]

The primary polarization direction of the luminescence in the disordered samples (2980 and 2983) is the [110] direction, orthogonal to that observed in sample 2979, which exhibited a spatially homogeneous luminescence distribution. As discussed in Sec. IV B, quantum confinement and strain are two competing factors in determining the direction of predominant polarization. The reversal of the QWR luminescence polarization anisotropy suggests:

(i) a substantial relaxation of strain in the In- and Ga-rich regions of the QWR in the BSL has occurred and/or
(ii) the formation of the domains and microstructure has affected the details of the cation diffusion that led to the In- and Ga-rich regions and subsequent growth of the QWR.

In the second possibility, the QWR array may be composed of sub-micron regions possessing QWRs whose widths and In composition vary markedly, leading to the broad multicomponent QWR peaks observed in Fig. 11. The existing data and complexity of the microstructure in CL imaging, however, does not allow for a quantitative assessment on these two possibilities.

## B. Time-resolved CL and excitation dependence of the QWR luminescence

As in the case of the excitation dependence of the homogeneous QWR sample (2979), we should expect marked variations in the QWR spectral lineshape of the optically inhomogeneous samples (2980 and 2983) upon varying the excitation intensity. Such results are shown in Fig. 14 for sample 2980, showing the QWR luminescence lineshape for varying beam currents. The electron beam was sharply focused to regions corresponding to typical *bright* and *dark* regions in the CL image of sample 2980. The lower energy side of the lineshapes is observed to dominate for a reduced beam current of 0.1 to ~1 nA, after which, the higher energy side of the spectrum has the larger intensity. We have deconvoluted the QWR lineshapes into two Gaussian peaks, $P_1$ and $P_2$, to further quantify the behavior of the CL intensity. The spectral line shape, $I(\hbar\omega)$, is represented as

$$I(\hbar\omega)=a_1\exp\left(-\frac{(\hbar\omega-E_1)^2}{\beta_1^2}\right)+a_2\exp\left(-\frac{(\hbar\omega-E_2)^2}{\beta_2^2}\right), \quad (8)$$

where $a_i$, $E_i$, and $\beta_i$ are the amplitude, energy position, and Guassian width of peak $P_i$ ($i=1,2$). The results of the fitting are shown in Fig. 14 as a solid line running through the data, and short- and long-dashed lines representing peaks $P_1$ and $P_2$, respectively. For the 14 spectra shown in Fig. 14, the mean values and standard deviations of $\beta_1$, $\beta_2$, and $E_1-E_2$ are 36±5, 49±9, and 64±7 meV, respectively. The fitting results for $a_1$, $E_1$, $a_2$, and $E_2$ are further plotted versus $e$-beam current in Fig. 15. As a result of band-filling, the ratio of $a_1/a_2$ increases with the probe current and indicates that the two luminescence features are within a close physical proximity of $\leqslant 1\ \mu$m (a carrier diffusion length) of each other. However, the rate of such an increase is faster in



Downloaded¬27¬Feb¬2007¬to¬132.72.138.1.¬Redistribution¬subject¬to¬AIP¬license¬or¬copyright,¬see¬http://jap.aip.org/jap/copyright.jsp

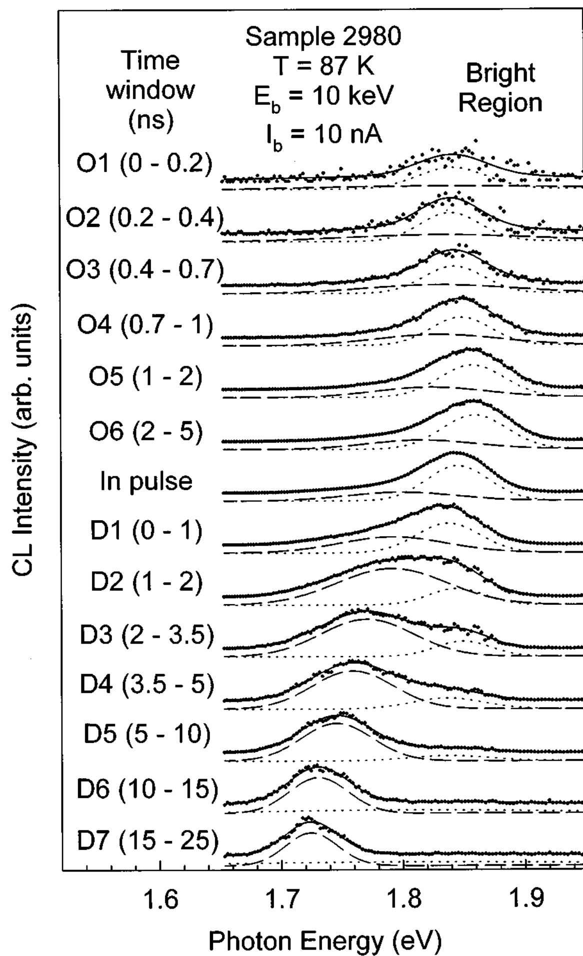


FIG. 16. Time-delayed CL spectra (sample 2980) shown with various onset (O*i*) and decay (D*i*) time windows. All spectra are renormalized to have about the same maximum peak height. The spectrum labeled *in pulse* was acquired in the center of the 50 ns *e*-beam pulse, after the system has nearly reached steady-state conditions. The decomposition of the spectra into two components ($P_1$ and $P_2$) using the model of Eq. (8) is shown in a fashion similar to that of Fig. 14.

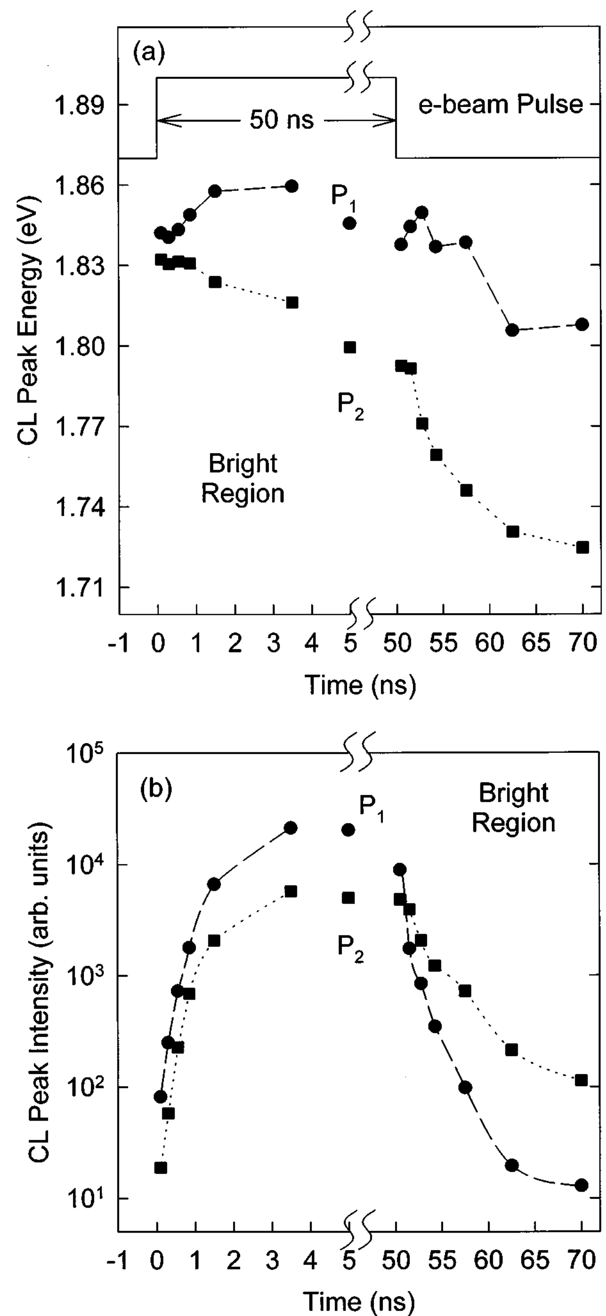


FIG. 17. (a) CL peak energy of peaks $P_1$ and $P_2$ vs time and (b) CL peak intensity of $P_1$ and $P_2$ vs time, relative to the 50 ns wide *e*-beam excitation pulse. The results are shown for a typical bright region.

the bright region than in the dark region. While peaks $P_1$ and $P_2$ shift towards higher energy with approximately the same rate as in sample 2979, the rate of the peak shift for $P_1$ is lower than that for $P_2$. The mechanism for these variations in the band-filling may relate to the presence of additional nonradiative recombination channels in the dark regions. The presence of such channels should increase the total recombination rate, thereby reducing the steady-state excitation density for a given beam current and rate of peak shift in the dark regions relative to that in the bright regions. The model discussed for sample 2979 in Secs. III and IV must be augmented to include spatial variations in the density of nonradiative centers when applying it to sample 2980. Moreover, local strain relaxation in close proximity to these defects will reduce the magnitude of the $v1-v2$ band splitting in the QWR, thereby also reducing the redistribution of holes and spatial separation of electrons and holes as the excitation is changed.

In order to better understand the details of the carrier relaxation and transfer between the regions giving rise to CL peaks $P_1$ and $P_2$, we have acquired time-delayed spectra of sample 2980, as shown in Fig. 16 for a typical bright region. Results for the dark regions are qualitatively similar. As in Sec. IV C, O1–O6 and D1–D7 represent spectra acquired in time windows corresponding to the onset and decay, respectively, of the 50 ns electron beam pulses. The spectra in Fig. 16 are also fit according to the model of Eq. (8), and the peaks are labeled in the same fashion as in Fig. 14. During the onset of luminescence in Fig. 16, the carriers initially



Downloaded¬27¬Feb¬2007¬to¬132.72.138.1.¬Redistribution¬subject¬to¬AIP¬license¬or¬copyright,¬see¬http://jap.aip.org/jap/copyright.jsp

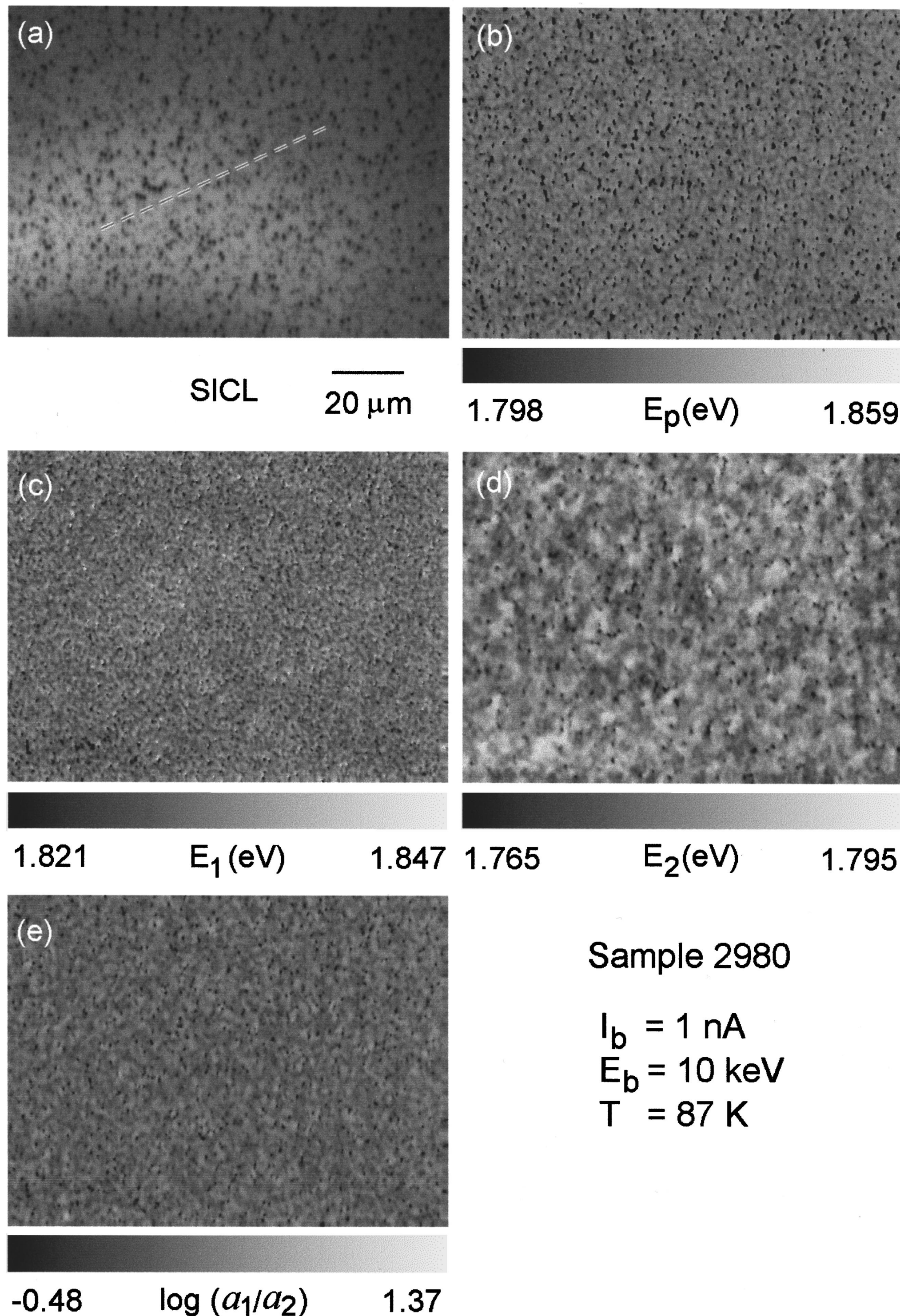


FIG. 18. CLWI consisting of (a) spectrally integrated CL (SICL) image and (b) spatial mapping of absolute CL peak energy ($E_p$), (c) peak energy of $P_1(E_1)$, (d) peak energy of $P_2(E_2)$, and (e) $\log(a_1/a_2)$. All images were taken over the same region and parameters were obtained by performing 640 $\times$480 fits, corresponding to the number of pixels in the image, to Eq. (8).

relax in to regions corresponding to the high-energy peak $P_1$ (long-dashed lines). Figure 17(a) shows a plot of the energy positions of $P_1$ and $P_2$ versus the onset and decay times. A small red-shift of 16 meV together with a gradual rise of the low-energy peak $P_2$ (short-dashed lines) is observed as the system proceeds from windows O1 to O6. The spectrum labeled *in pulse* is again acquired with the window centered in the middle of the 50 ns $e$-beam pulse, yielding a lineshape representative of a steady-state excitation with $I_b = 10$ nA, as in Fig. 14. In the decay phase, the relative intensity of $P_1$ and $P_2$ reverses [see Fig. 17(b)] as carriers thermalize into the lower energy $P_2$ states. Carrier feeding into the $P_2$ states is accomplished by thermal re-emission from the higher energy QWR states of $P_1$, diffusive trans-



Downloaded¬27¬Feb¬2007¬to¬132.72.138.1.¬Redistribution¬subject¬to¬AIP¬license¬or¬copyright,¬see¬http://jap.aip.org/jap/copyright.jsp

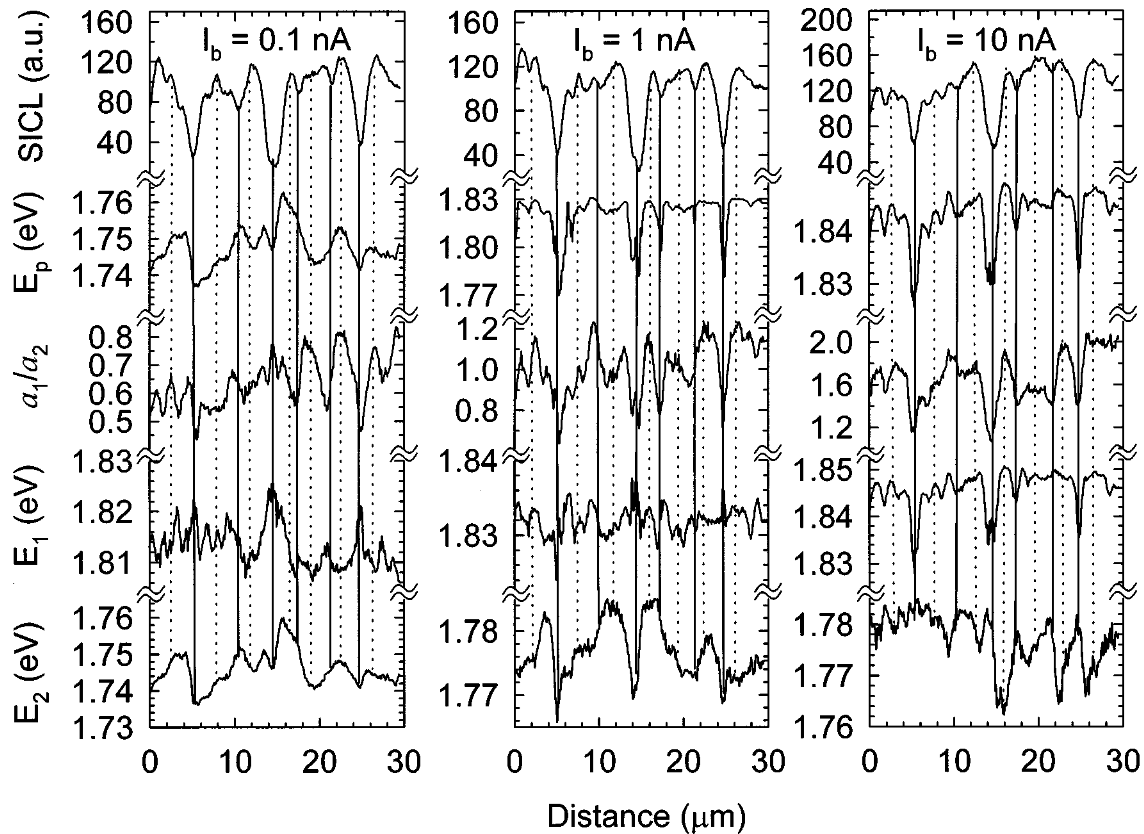


FIG. 19. Line scan analysis of the CLWI results taken along an arbitrary line indicated with a dash line in Fig. 18. The line scan analysis is shown for CLWI images taken for beam currents of 0.1, 1, and 10 nA.

port over surrounding barriers, and carrier collections into the $P_2$ states. It is remarkable that the initial carrier relaxation occurs into QWR regions exhibiting the high-energy $P_1$ states for short onset times of $\sim 100$ ps. This shows the existence of barriers inhibiting initially diffusive transport and collection into the low-energy $P_2$ regions. The red-shift of both $P_1$ and $P_2$ states is evident in Fig. 17(a) during the decay since the carrier densities and quasi-Fermi level splitting reduce as the system proceeds towards equilibrium.

The time-delayed spectra corroborate with the excitation-dependent data of Fig. 14. Carrier transfer and exchange between regions corresponding to the $P_1$ and $P_2$ emissions occur on a length scale less than $\sim 1$ μm. The presence of these two emission strongly suggest the possibility of two different QWR widths and/or compositions that would give rise to different excitonic energies. The disorder inducing the microstructure during the $In_{0.49}Ga_{0.51}P$ growth should also affect the details of phase separation and spinodal decomposition during the initial phases of the $(InP)_2/(GaP)_2$ BSL growth. The observation of a partially disordered QWR array, giving rise to two or more distinct emissions is, to our knowledge, a new observation in the SILO work. An even more complicated situation is observed for the case of sample 2983, whose CL spectrum (Fig. 11) reveals a broad BSL peak composed of many QWR-like components. Since all three samples were grown under nominally the same growth conditions, small variations in the growth conditions and substrate quality significantly influence the microstructure and concomitant optical properties.

### C. CL wavelength imaging of spectral and spatial correlations in the QWR microstructure

To further examine the effect of defects on the optical properties of the BSL structure, we employed a variation of the CL imaging technique that allows for simultaneous acquisition of spatial and spectral information. Previous studies have shown that CL wavelength imaging or CLWI is very useful in studying the optical properties in the presence of defects or strain.[25] In this study, a series of monochromatic CL images with wavelength ranging from 650 to 740 nm were taken of sample 2980. Figures 18(a) and 18(b) show the mapping of the spectrally integrated CL (SICL) intensity and energy of maximum CL intensity ($E_P$) over a region of 128 μm×94 μm under a probe current of 1 nA. The mapping of energy into a gray-scale representation is shown by the gray bar indicating the energy scale. The deconvolution results, $E_1$, $E_2$, and $\log(a_1/a_2)$ from the model of Eq. (8) are also mapped over the same region as shown in Figs. 18(c)–18(e). The ratio of $a_1/a_2$ represents the relative intensity of $P_1$ and $P_2$. CLWI has also been performed for various other probe currents (0.1–10 nA), yielding similar results.



Downloaded¬27¬Feb¬2007¬to¬132.72.138.1.¬Redistribution¬subject¬to¬AIP¬license¬or¬copyright,¬see¬http://jap.aip.org/jap/copyright.jsp

In order to illustrate the correlation existing amongst the images in Fig. 18, line scans of the imaging data are shown in Fig. 19 for probe currents of 0.1, 1 and 10 nA, corresponding to low-, medium-, and high-excitation conditions, respectively. The spectrally integrated CL (SICL) intensity, the energy corresponding to the peak position of maximum intensity for the total QWR CL spectrum ($E_p$), the ratio of $a_1/a_2$, and the peak energies of $P_1$ and $P_2$ ($E_1$ and $E_2$) are plotted as a function of the distance taken along an arbitrary line. Vertical dashed and dotted lines are shown as a guide for the eye in assessing the correlations. For all excitation conditions, the dips in SICL (i.e., dark regions in the CL images) correspond to dips in the CL peak energy and $a_1/a_2$ ratio. This is consistent with the idea that dark regions contain a higher defect density which leads to a higher nonradiative recombination rate. In dark regions, this further reduces the band-filling, leading to a local red-shift and enhancement of the $P_2$ emission relative to $P_1$. The red-shift in dark regions could also be caused by a local reduction in the compressive strain in the BSL caused by underlying cellular and CuPt-like domain related defects in the $In_{0.49}Ga_{0.51}P$ barriers. For all three current conditions, the reduced $a_1/a_2$ ratio near defects demonstrates a marked reduction in the nonlinear optical properties near the defect dark regions. Likewise, the energy positions of the $P_1$ and $P_2$ peaks, denoted by $E_1$ and $E_2$, show interesting correlations within the line scan. As the beam current is increased, the energy difference $E_1-E_2$ shows an enhanced sensitivity near regions away from defects (i.e., bright regions). That is, $E_1-E_2$ increases more rapidly away from the defects, again indicating that band-filling in higher-quality QWR regions (bright regions) enables a more-rapid blue-shifting of the higher energy $P_1$ peaks. This is also consistent with the notion that an enhanced mobility and diffusive transport of carriers occurs in regions possessing fewer defects, thereby facilitating the collection of carriers in QWR regions exhibiting the $P_1$ emission.

## VI. CONCLUSION

In conclusion, we have performed a detailed study of the band-filling and polarization anisotropy of $(InP)_2/(GaP)_2$ QWRs using time-resolved CL and linearly polarized CL. The BSL, owing to the SILO process, spontaneously orders into QWR arrays. We have calculated the excitation-dependent polarization anisotropy and CL energy shifts with a $\mathbf{k}\cdot\mathbf{p}$ model that incorporates both strain and quantum confinement. The calculations confirm a strong interplay between band-filling and $e-h$ wave function overlap, which leads to very interesting and possibly useful nonlinear optical and polarization properties. The linearly polarized CL and excitation-dependent CL data are consistent with the calculations. Time-resolved CL measurements show a rapid capture of carriers from the $In_{0.49}Ga_{0.51}P$ barrier on a scale of less than $\sim 100$ ps. Time-delayed spectra have been examined to connect changes in CL linewidth and position with band-filling in the QWR during the *onset* and *decay* of the electron beam pulses. Experiments performed at various temperatures show that thermal activation of carriers in the QWR and transfer to and from the $In_{0.49}Ga_{0.51}P$ barriers plays an important role in determining the measured lifetimes. A decrease in lifetime at higher temperatures may be caused by thermal re-emission from the QWR to the barrier.

The optical properties and crystal quality of the $In_{0.49}Ga_{0.51}P$ barriers and $(InP)_2/(GaP)_2$ BSL strongly depended on the growth and sample surface conditions. Samples exhibiting nonuniform bright and dark regions in the CL imaging show large spatial variations in the phase-space filling and nonlinear optical properties. These defects are associated with

(i) the starting GaAs substrate or
(ii) the initial stages of $In_{0.49}Ga_{0.51}P$ growth on GaAs in which In-rich regions at the GaAs surface form.

The subsequent growth of a $(InP)_2/(GaP)_2$ BSL over the $In_{0.49}Ga_{0.51}P$ buffer layer resulted in SILO QWRs. CL imaging showed that dark-defect regions arising in the GaAs, QWR, and $In_{0.49}Ga_{0.51}P$ emissions correlate spatially. A narrow luminescence lineshape for the QWR emission was observed for a sample exhibiting a high degree of homogeneity in the CL imaging.

Two samples exhibiting disorder in the CL imaging show a broadening of the QWR luminescence lineshape into two or more components. A detailed study of the excitation dependence and spatial correlations of these components has been performed for a BSL sample which exhibits two QWR-like components in its CL spectrum. Time-resolved CL and excitation-dependent CL experiments show that diffusive transport and thermalization of carriers occur between two distinct QWR regions giving rise to the two components comprising the QWR spectral lineshape. CL wavelength imaging shows that defects existing in the barrier reduce the sensitivity of the QWR to band-filling, owing to the enhancement of the nonradiative recombination rate and local reduction of the steady-state carrier density. In conclusion, these results demonstrate the need to minimize the defect density and maximize the homogeneity in SILO QWR samples in order to optimize the nonlinear optical effects associated with phase-space filling.

## ACKNOWLEDGMENTS

This work was supported by the U.S. Army Research Office and the National Science Foundation (RIA-ECS). The authors wish to thank P. Colter and S. M. Vernon of Spire Corporation for use of their samples.

## APPENDIX A

The Luttinger–Kohn and Pikus–Bir Hamiltonian, $\mathscr{H}_T(\mathbf{k})=\mathscr{H}_{\rm LK}(\mathbf{k})+\mathscr{H}_{\rm PB}$, for the valence bands can be expressed by a $8\times 8$ matrix:



Downloaded¬27¬Feb¬2007¬to¬132.72.138.1.¬Redistribution¬subject¬to¬AIP¬license¬or¬copyright,¬see¬http://jap.aip.org/jap/copyright.jsp

$$\mathscr{H}_T(k_x,k_y,k_z)=\begin{bmatrix} E_g+E_k & 0 & 0 & 0 & 0 & 0 & 0 & 0 \\ 0 & E_g+E_k & 0 & 0 & 0 & 0 & 0 & 0 \\ 0 & 0 & P+Q & S & R & 0 & \frac{S}{\sqrt{2}} & \sqrt{2}R \\ 0 & 0 & S^* & P-Q & 0 & R & -\sqrt{2}Q & -\sqrt{\frac{3}{2}}S \\ 0 & 0 & R^* & 0 & P-Q & -S & -\sqrt{\frac{3}{2}}S^* & \sqrt{2}Q \\ 0 & 0 & 0 & R^* & -S^* & P+Q & -\sqrt{2}R^* & \frac{S^*}{\sqrt{2}} \\ 0 & 0 & \frac{S^*}{\sqrt{2}} & -\sqrt{2}Q & -\sqrt{\frac{3}{2}}S & -\sqrt{2}R & -\Delta+P' & 0 \\ 0 & 0 & \sqrt{2}R^* & -\sqrt{\frac{3}{2}}S^* & \sqrt{2}Q & \frac{S}{\sqrt{2}} & 0 & -\Delta+P' \end{bmatrix} \begin{matrix} |u_{e,1}\rangle \\ |u_{e,2}\rangle \\ \left|\frac{3}{2},\frac{3}{2}\right\rangle \\ \left|\frac{3}{2},\frac{1}{2}\right\rangle \\ \left|\frac{3}{2},-\frac{1}{2}\right\rangle \\ \left|\frac{3}{2},-\frac{3}{2}\right\rangle \\ \left|\frac{1}{2},\frac{1}{2}\right\rangle \\ \left|\frac{1}{2},-\frac{1}{2}\right\rangle \end{matrix}, \quad \text{(A1)}$$

where

$$E_k=\frac{\hbar^2}{2m_e^*}(k_x^2+k_y^2+k_z^2),$$

$$P=-\frac{\hbar^2}{2m_0}\gamma_1(k_x^2+k_y^2+k_z^2)-a(\epsilon_{xx}+\epsilon_{yy}+\epsilon_{zz}),$$

$$Q=\frac{\hbar^2}{2m_0}\gamma_2(2k_z^2-k_x^2-k_y^2)-\frac{b}{2}(2\epsilon_{zz}-\epsilon_{xx}-\epsilon_{yy}),$$

$$S=\frac{\hbar^2}{2m_0}2\sqrt{3}\gamma_3(k_x-ik_y)k_z-d(\epsilon_{zx}-i\epsilon_{yz}), \quad \text{(A2)}$$

$$R=\frac{\hbar^2}{2m_0}\sqrt{3}\gamma_2(k_x^2-k_y^2)-i\frac{\hbar^2}{2m_0}2\sqrt{3}\gamma_3k_xk_y - \frac{\sqrt{3}}{2}b(\epsilon_{xx}-\epsilon_{yy})+id\epsilon_{xy},$$

$$P'=-\frac{\hbar^2}{2m_0}A_0(k_x^2+k_y^2+k_z^2)-a(\epsilon_{xx}+\epsilon_{yy}+\epsilon_{zz}),$$

with basis functions of $|u_{e,1,2}\rangle$ and $|J,m_J\rangle$ as

$$|u_{e,1}\rangle=|S\uparrow\rangle,$$

$$|u_{e,2}\rangle=|S\downarrow\rangle,$$

$$\left|\frac{3}{2},\frac{3}{2}\right\rangle=-\frac{1}{\sqrt{2}}|(X+iY)\uparrow\rangle,$$

$$\left|\frac{3}{2},\frac{1}{2}\right\rangle=-\frac{1}{\sqrt{6}}|(X+iY)\downarrow\rangle+\sqrt{\frac{2}{3}}|Z\uparrow\rangle,$$

$$\left|\frac{3}{2},-\frac{1}{2}\right\rangle=\frac{1}{\sqrt{6}}|(X-iY)\uparrow\rangle+\sqrt{\frac{2}{3}}|Z\downarrow\rangle,$$

$$\left|\frac{3}{2},-\frac{3}{2}\right\rangle=\frac{1}{\sqrt{2}}|(X-iY)\downarrow\rangle,$$

$$\left|\frac{1}{2},\frac{1}{2}\right\rangle=\frac{1}{\sqrt{3}}|(X+iY)\downarrow\rangle+\frac{1}{\sqrt{3}}|Z\uparrow\rangle,$$

$$\left|\frac{1}{2},-\frac{1}{2}\right\rangle=-\frac{1}{\sqrt{3}}|(X-iY)\uparrow\rangle+\frac{1}{3}|Z\downarrow\rangle. \quad \text{(A3)}$$


[1] A. Yariv, Appl. Phys. Lett. **53**, 1033 (1988).
[2] H. Zarem, K. Vahala, and A. Yariv, IEEE J. Quantum Electron. **QE-25**, 705 (1989).
[3] Y. Arkawa and H. Sakaki, Appl. Phys. Lett. **40**, 939 (1982).
[4] M. Tsuchiya, J. M. Gaines, R. H. Yan, R. J. Simes, P. O. Holtz, L. A. Coldren, and P. M. Petroff, Phys. Rev. Lett. **62**, 466 (1989).
[5] J. M. Gaines, P. M. Petroff, H. Kroemer, R. J. Simes, R. S. Geels, and J. H. English, J. Vac. Sci. Technol. B **6**, 1378 (1988).
[6] E. Kapon, M. C. Tamargo, and D. M. Hwang, Appl. Phys. Lett. **50**, 347 (1987).
[7] E. Kapon, D. M. Hwang, and R. Bhat, Phys. Rev. Lett. **63**, 430 (1989).
[8] W. J. Schaff, in ''Device Applications of Strained-layer Epitaxy'' edited by R. K. Willardson and A. C. Beer, *Semiconductors and Semimetals* (Academic, New York, 1991), Vol. 33, pp. 73–138.
[9] A. Madhukar, K. C. Rajkumar, and P. Chen, Appl. Phys. Lett. **62**, 1547 (1993), and references therein.
[10] K. C. Rajkumar, A. Madhukar, K. Rammohan, D. H. Rich, P. Chen, and L. Chen, Appl. Phys. Lett. **63**, 2905 (1993).
[11] A. Konkar, K. C. Rajkumar, Q. Xie, P. Chen, A. Madhukar, H. T. Lin, and D. H. Rich, J. Cryst. Growth **150**, 311 (1995).
[12] K. C. Hsieh, J. N. Baillargeon, and K. Y. Cheng, Appl. Phys. Lett. **57**, 2244 (1990).
[13] K. Y. Cheng, K. C. Hsieh, and J. N. Baillargeon, Appl. Phys. Lett. **60**, 2892 (1992).
[14] P. J. Pearah, E. M. Stellini, A. C. Chen, A. M. Moy, K. C. Hsieh, and K. Y. Cheng, Appl. Phys. Lett. **62**, 729 (1993).
[15] A. C. Chen, A. M. Moy, P. J. Pearah, K. C. Hsieh, and K. Y. Cheng, Appl. Phys. Lett. **62**, 1359 (1993).
[16] K. C. Hsieh and K. Y. Cheng, Mater. Res. Soc. Symp. Proc. **379**, 145 (1995).
[17] Y. Tang, H. T. Lin, D. H. Rich, P. Colter, and S. M. Vernon, Phys. Rev. B **53**, R10 501 (1996).
[18] Y. Tang, K. Rammohan, H. T. Lin, D. H. Rich, P. Colter, and S. M.





Downloaded¬27¬Feb¬2007¬to¬132.72.138.1.¬Redistribution¬subject¬to¬AIP¬license¬or¬copyright,¬see¬http://jap.aip.org/jap/copyright.jsp

Vernon, Mater. Res. Soc. Symp. Proc. **379**, 165 (1995).
[19] P. J. Pearah, A. C. Chen, A. M. Moy, K. C. Hsieh, and K. Y. Cheng, IEEE J. Quantum Electron. **30**, 608 (1994).
[20] A. Mascarenhas, R. G. Alonso, G. S. Horner, S. Froyen, K. C. Hsieh, and K. Y. Cheng, Phys. Rev. B **48**, 4907 (1993).
[21] P. R. Hageman, A. van Geelen, W. Gabrielse, G. J. Bauhuis, and L. J. Giling, J. Cryst. Growth **125**, 336 (1992).
[22] M. C. DeLong, P. C. Taylor, and J. M. Olson, Appl. Phys. Lett. **57**, 620 (1990).
[23] D. H. Rich, A. Ksendzov, R. W. Terhune, F. J. Grunthaner, B. A. Wilson, H. Shen, M. Dutta, S. M. Vernon, and T. M. Dixon, Phys. Rev. B **43**, 6836 (1991).
[24] M. Grundmann, J. Christen, D. Bimberg, A. Hashimoto, T. Fukunaga, and N. Watanabe, Appl. Phys. Lett. **58**, 2090 (1991).
[25] K. Rammohan, Y. Tang, D. H. Rich, R. S. Goldman, H. H. Wieder, and K. L. Kavanagh, Phys. Rev. B **51**, 5033 (1995); K. Rammohan, D. H. Rich, R. S. Goldman, J. Chen, H. H. Wieder, and K. L. Kavanagh, Appl. Phys. Lett. **66**, 869 (1995).
[26] D. Bimberg, H. Munzel, A. Steckenborn, and J. Christen, Phys. Rev. B **31**, 7788 (1985).
[27] F. H. Pollak, *Semiconductors and Semimetals*, edited by R. K. Willardson and A. C. Beer (Wiley, New York, 1990), Vol. 32, pp. 17–53.
[28] K. B. Wong, M. Jaros, and J. P. Hagon, Phys. Rev. B **35**, 2463 (1987).
[29] B. Jonsson and S. T. Eng, IEEE J. Quantum Electron. **26**, 2025 (1990).
[30] D. H. Rich, H. T. Lin, and A. Larsson, J. Appl. Phys. **77**, 6557 (1995).
[31] A. Mascarenhas, S. Kurtz, A. Kibbler, and J. M. Olson, Phys. Rev. Lett. **63**, 2108 (1989).
[32] D. J. Friedman, G. S. Hormer, S. R. Kurtz, K. A. Bertness, J. M. Olson, and J. Moreland, Appl. Phys. Lett. **65**, 878 (1994).
[33] S. H. Wei and A. Zunger, Appl. Phys. Lett. **58**, 2684 (1991); **56**, 662 (1990).
[34] R. P. Schneider, Jr., R. P. Bryan, E. D. Jones, and J. A. Lott, Appl. Phys. Lett. **63**, 1240 (1993).
[35] M. Prasad, O. E. Martinez, and C. S. Menoni, J. Electron. Mater. **23**, 359 (1994).
[36] U. Jahn, J. Menniger, R. Hey, and H. T. Grahn, Appl. Phys. Lett. **64**, 2382 (1994).
[37] K. Rammohan, H. T. Lin, D. H. Rich, and A. Larsson, J. Appl. Phys. **78**, 6687 (1995).
[38] A similar situation is observed for $e-h$ plasma transport in partially relaxed $In_xGa_{1-x}As$/GaAs multiple quantum wells in Ref. 30.
[39] B. Deveaud, J. Shah, T. C. Damen, and W. T. Tsang, Appl. Phys. Lett. **52**, 1886 (1988).
[40] We note that the coalescence of 3D islands in the $In_{0.49}Ga_{0.51}P$ growth could also lead to the presence of cellular-type boundaries in CL imaging, as this has been observed in CL studies of ZnSe/GaAs(001); see H. T. Lin, D. H. Rich, and D. B. Wittry, J. Appl. Phys. **75**, 8080 (1994).
[41] T. Suzuki, A. Gomyo, and S. Iijima, J. Cryst. Growth **93**, 396 (1988).



Downloaded¬27¬Feb¬2007¬to¬132.72.138.1.¬Redistribution¬subject¬to¬AIP¬license¬or¬copyright,¬see¬http://jap.aip.org/jap/copyright.jsp